

Towards non-parametric fiber-specific T_1 relaxometry in the human brain

A. Reymbaut^{1,2,*}, J. Critchley³, G. Durighel³, T. Sprenger^{4,5}, M. Sughrue⁶, K. Bryskhe², and D. Topgaard^{1,2}

¹Department of Physical Chemistry,
Lund University, Lund, Sweden

²Random Walk Imaging AB, Lund, Sweden

³Spectrum Medical Imaging, Sydney, Australia

⁴Karolinska Institute, Stockholm, Sweden

⁵GE Healthcare, Stockholm, Sweden

⁶Charlie Teo Foundation, Sydney, Australia

(Dated: November 15, 2021)

Purpose: To estimate fiber-specific T_1 values, *i.e.* proxies for myelin content, in heterogeneous brain tissue.

Methods: A diffusion- T_1 correlation experiment was carried out on an *in vivo* human brain using tensor-valued diffusion encoding and multiple repetition times. The acquired data was inverted using a Monte-Carlo inversion algorithm that retrieves non-parametric distributions $\mathcal{P}(\mathbf{D}, R_1)$ of diffusion tensors and longitudinal relaxation rates $R_1 = 1/T_1$. Orientation distribution functions (ODFs) of the highly anisotropic components of $\mathcal{P}(\mathbf{D}, R_1)$ were defined to visualize orientation-specific diffusion-relaxation properties. Finally, Monte-Carlo density-peak clustering (MC-DPC) was performed to quantify fiber-specific features and investigate microstructural differences between white-matter fiber bundles.

Results: Parameter maps corresponding to $\mathcal{P}(\mathbf{D}, R_1)$'s statistical descriptors were obtained, exhibiting the expected R_1 contrast between brain-tissue types. Our ODFs recovered local orientations consistent with the known anatomy and indicated possible differences in T_1 relaxation between major fiber bundles. These differences, confirmed by MC-DPC, were in qualitative agreement with previous model-based works but seem biased by the limitations of our current experimental setup.

Conclusions: Our Monte-Carlo framework enables the non-parametric estimation of fiber-specific diffusion- T_1 features, thereby showing potential for characterizing developmental or pathological changes in T_1 within a given fiber bundle, and for investigating inter-bundle T_1 differences.

I. INTRODUCTION

While diffusion MRI has provided enhanced sensitivity to tissue microstructure *in vivo* by capturing the translational motion of water molecules diffusing in biological tissue,^{1–4} diffusion-relaxation MRI (drMRI) additionally reports on the local chemical composition of the aqueous phase.^{5–12} For instance, the longitudinal relaxation time T_1 informs on molecular dynamics¹³ and on the presence of paramagnetic species¹⁴ in simple liquids. *In vivo*, it is mainly determined by cross relaxation, magnetization transfer and spin diffusion with macromolecules in general^{15–17} and myelin lipids in particular,^{18–22} as well as by the interplay between relaxation and diffusion.²³ However, microstructural studies have been hindered by the fact that the measured drMRI signal is only sensitive to the voxel-averaged diffusion-relaxation profile, with typical cubic-millimeter voxels comprising multiple cell types and the extra-cellular space.^{24–28}

Two strategies were explored to alleviate the lack of specificity of the drMRI signal. On the one hand, multiple models and signal representations have been developed to relate either the diffusion- T_2 ^{29–31} or diffusion- T_1 ^{6,7,32} MRI signal to the voxel content. However, models/signal representations rely on compartmental/functional assumptions that may disagree with the underlying tissue microstructure.^{33–35} On the other hand, ‘tensor-valued’ diffusion encoding gradient waveforms have enhanced the specificity of the data itself

by targeting specific features of the intra-voxel diffusion profile.^{36–41} Indeed, such measurements typically use four acquisition dimensions - the trace b (size), normalized anisotropy $b_\Delta \in [-0.5, 1]$ (shape) and orientation (Θ, Φ) of an axisymmetric encoding tensor \mathbf{b} ^{3,42,43} - to probe the four dimensions of microscopic axisymmetric diffusion tensors, *i.e.* their isotropic diffusivity D_{iso} , normalized anisotropy $D_\Delta \in [-0.5, 1]$ and orientation (θ, ϕ) .^{44,45} Tensor-valued diffusion acquisition schemes have since been used to further investigate signal representations^{39,46,47} and models.^{48–53}

While inversion of the diffusion-relaxation NMR signal is already common practice in the porous media field,^{54–57} the advent of ‘tensor-valued’ diffusion-relaxation correlation measurements has resulted in the development of non-parametric Monte-Carlo signal inversion algorithms of the diffusion⁵⁸ and diffusion- T_1 - T_2 ¹¹ MRI signals in porous media, and of the diffusion⁵⁹ and diffusion- T_2 ¹² MRI signals in the *in vivo* brain. Although noise-sensitive,³⁵ these algorithms do not rely on any compartmental/functional assumption regarding the voxel content, nor on constraints regarding data compression⁶⁰ or the density of the acquisition sampling scheme.^{61–65} They also do not consider any regularization to guide the search for a suitable solution to the inverse problem.^{66–69} Enhanced by methods aiming to visualize and quantify fiber-specific properties, even in fiber-crossing areas of the white matter (60 to 90% of voxels in a typical whole-brain imaging experiment⁷⁰),

Monte-Carlo signal inversions have been shown to yield critical sensitivity and specificity to fiber-specific T_2 values.^{71–73} However, this work has yet to be extended to fiber-specific T_1 -values, which are of particular interest to evaluate changes in bundle-specific myelin contents,⁷⁴ relevant to the study of neurodevelopment, plasticity, aging and neurological disorders.^{75–77} Indeed, T_1 contrast is sensitive to myelin,^{18–22} like many other contrasts^{78,79} such as T_2 ,^{80–86} T_2^* ^{87–89} and magnetization transfer.^{82,90} Importantly, note that none of these contrasts are ‘specific’ to myelin.⁷⁹

In this work, we leverage non-parametric distributions $\mathcal{P}(\mathbf{D}, R_1)$ of diffusion tensors \mathbf{D} and longitudinal relaxation rates $R_1 = 1/T_1$ obtained *via* Monte-Carlo inversion of a diffusion- T_1 weighted *in vivo* human-brain dataset to resolve sub-voxel diffusion- R_1 components. We first estimate parameter maps of these distributions’ statistical descriptors and extract orientation-resolved T_1 values within the pool of highly anisotropic components output by the Monte-Carlo inversion algorithm. These T_1 values are then color-mapped onto non-parametric orientation distribution functions (ODFs)^{71,72} and quantified in terms of median value and precision using orientational clusters obtained *via* Monte-Carlo density-peak clustering (MC-DPC).⁷³ In particular, these novel tools enable to identify significant differences with respect to T_1 relaxation between major white-matter bundles. After describing how our *in vivo* human-brain data was acquired in Section II A, we lay down the theory underlying the Monte-Carlo signal inversion algorithm, the statistical descriptors of $\mathcal{P}(\mathbf{D}, R_1)$, and our ODFs in Section II B, and detail the MC-DPC procedure in Section II C. We then present our results in Section III and discuss them in Section IV, before concluding in Section V.

We emphasize that this work is merely a proof of concept for non-parametric fiber-specific T_1 relaxometry. Firstly, vast improvements could be brought to our experimental setup, as detailed in Sections II A and IV. Second, better matching between the output of our Monte-Carlo framework and plausible white-matter tracts would be yielded upon integrating tractography^{91–98} into our analysis pipeline.

II. METHODS

A. In vivo human-brain data

Data collection was approved by the Spectrum Medical Imaging local ethics committee. A healthy volunteer was scanned on a 3T GE 750w equipped with a 32-channel receiver head and neck GEM coils (only 12-16 channels used for head) using a prototype GE multidimensional diffusion (MDD) spin-echo sequence with EPI readout, echo time $\tau_E = 120$ ms, FOV=240x240x12 mm³, voxel-size=3x3x3 mm³, fat-saturation (fat-sat) pulses,⁹⁹ and ASSET acceleration factor=2, customized for tensor-valued diffusion encoding^{46,100} and variable repetition

time τ_R . Tensor-valued diffusion encoding was performed with numerically optimized¹⁰¹ Maxwell-compensated¹⁰² waveforms. We also attempted to match their frequency contents.¹⁰³ The same tensor-valued diffusion-weighted sequence was repeated for $\tau_R = 1, 2$ and 5 s. The dimensions of the resulting 20-minute 363-point acquisition scheme, shown in Figure 1, match those of $\mathcal{P}(\mathbf{D}, R_1)$. The signal-to-noise ratio of this dataset was estimated across voxels of the corona radiata by computing the mean-to-standard-deviation ratio of the spherically encoded diffusion signal at $b = 0.1$ ms/ μm^2 (see Supplemental Material of Ref. 100). It equals 20 at $\tau_R = 1$ s and 40 at $\tau_R = 5$ s.

As indicated by the aforementioned FOV and voxel size, only four axial slices were acquired so that to limit the acquisition time. While an inversion-recovery slice-shuffling sequence could drastically reduce acquisition time,^{8,9} our prototype sequence is currently limited to sequential slices.

B. Non-parametric Monte-Carlo inversion

1. Signal fitting and bootstrapping

We used a modified version of the 5D Monte-Carlo inversion algorithm found in Ref. 12 (pioneered by Ref. 54) to analyze the diffusion- R_1 dataset described in Section II A. Let us consider axisymmetric diffusion tensors, parametrized by their axial diffusivity D_{\parallel} , radial diffusivity D_{\perp} and orientation (θ, ϕ) . An alternative parametrization includes the isotropic diffusivity $D_{\text{iso}} = (D_{\parallel} + 2D_{\perp})/3$ and normalized anisotropy $D_{\Delta} = (D_{\parallel} - D_{\perp})/(D_{\parallel} + 2D_{\perp}) \in [-0.5, 1]$.^{38,44,45} Our Monte-Carlo inversion technique retrieves non-parametric 5D intra-voxel distributions $\mathcal{P}(\mathbf{D}, R_1) \equiv \mathcal{P}(D_{\parallel}, D_{\perp}, \theta, \phi, R_1)$ by fitting a set of diffusion- T_1 weighted signals with a finite weighted sum of N components $(\mathbf{D}_n, R_{1,n}) \equiv (D_{\parallel,n}, D_{\perp,n}, \theta_n, \phi_n, R_{1,n})$, with $1 \leq n \leq N = 50$. Given that the T_1 -weighting of the dataset detailed in Section II A is provided through a spin-echo sequence with constant echo time τ_E and variable repetition time τ_R , the inversion algorithm inverts the following discretized signal equation¹⁰⁴

$$\mathcal{S}_m = \sum_{n=1}^N w_n \exp(-\mathbf{b}_m : \mathbf{D}_n) \times [1 - 2 \exp([\tau_E/2 - \tau_{R,m}]R_{1,n}) + \exp(-\tau_{R,m}R_{1,n})], \quad (1)$$

where \mathcal{S}_m is the m^{th} acquired signal, w_n is the weight of the n^{th} component, \mathbf{b} is the diffusion-encoding tensor (b-tensor)^{42,43} from tensor-valued diffusion encoding,^{36–41} and “:” is the Frobenius inner product. The weights w_n are normalized so that $\sum_{n=1}^N w_n = \mathcal{S}_0 = \mathcal{S}(\mathbf{b} = \mathbf{0}, \tau_R \rightarrow +\infty)$. For axisymmetric b-tensors, the Frobenius inner product writes³⁸ $\mathbf{b} : \mathbf{D} = bD_{\text{iso}}[1 + 2b_{\Delta}D_{\Delta}P_2(\cos \beta)]$, where $P_2(x) = (3x^2 - 1)/2$ is the second Legendre polynomial and $\cos \beta = \cos \Theta \cos \theta + \sin \Theta \sin \theta \cos(\Phi - \phi)$ is

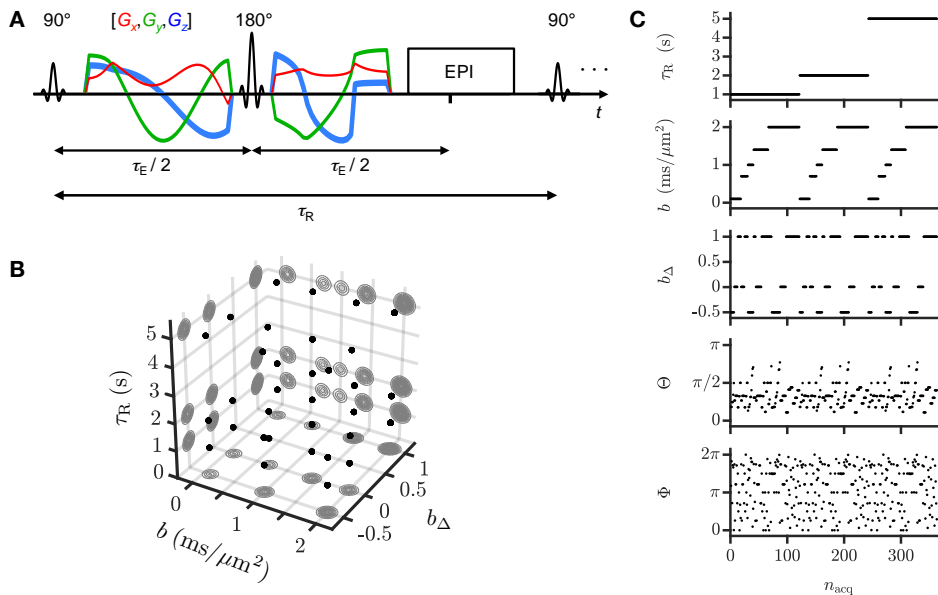


Figure 1. Visualization of our acquisition scheme. (A) Spin-echo sequence with EPI readout customized for tensor-valued diffusion encoding and variable repetition time τ_R . (B) 5D grid-like acquisition scheme where black points indicate the acquisition points in the 3D subspace of repetition time τ_R , b-tensor size b and b-tensor shape $b_\Delta \in [-0.5, 1]$. The number of b-tensor orientations (Θ, Φ) for each point is illustrated by the projected contours. (C) Acquisition parameters as a function of sorted acquisition point index n_{acq} .

the cosine of the shortest angle β between the main axis (Θ, Φ) of \mathbf{b} and the main axis (θ, ϕ) of \mathbf{D} .

A short-hand notation of Equation 1 reads

$$\mathbf{S} = \mathbf{K}\mathbf{w}, \quad (2)$$

where \mathbf{S} is the column vector containing the acquired signals \mathcal{S}_m , \mathbf{K} is the inversion kernel matrix containing the signal decays and \mathbf{w} is the column vector containing the weights w_n of the components $(\mathbf{D}_n, R_{1,n})$. The Monte-Carlo inversion algorithm randomly samples such components within the following ranges, $D_{\parallel}, D_{\perp} \in [5 \times 10^{-3}, 5] \mu\text{m}^2/\text{ms}$, $\cos \theta \in [0, 1]$, $\phi \in [0, 2\pi[$ and $R_1 \in [0.1, 2] \text{s}^{-1}$, and estimates the associated vector \mathbf{w} quantifying the components' propensity to fit the acquired signals *via* non-negative least-squares fitting.^{60,68,69,105,106}

$$\mathbf{w} = \underset{\mathbf{w}' \geq 0}{\text{argmin}} \|\mathbf{S} - \mathbf{K}\mathbf{w}'\|_2^2, \quad (3)$$

where $\|\cdot\|_2$ denotes the L_2 norm. This process is repeated iteratively following a quasi-genetic filtering detailed in Refs. 11, 12, 58, and 59. Embracing the inherent ill-conditioning of Laplace inversion problems, we performed bootstrapping with replacement¹⁰⁷ on the data and estimated for each voxel an ensemble of $N_b = 96$ plausible sets of components, also called "bootstrap solutions", each denoted by $\{(D_{\parallel,n}, D_{\perp,n}, \theta_n, \phi_n, R_{1,n}, w_n)\}_{1 \leq n \leq N=20}$. We then computed statistical descriptors of $\mathcal{P}(\mathbf{D}, R_1)$ for each bootstrap solution and calculated the median of each statistical descriptor across bootstrap solutions (see Section II B 2).

2. Statistical descriptors and binning

The final solution of the Monte-Carlo inversion algorithm, $\mathcal{P}(\mathbf{D}, R_1)$, can be understood as the median of the solutions obtained for each bootstrap solution, $\mathcal{P}_{n_b}(\mathbf{D}, R_1)$, with $1 \leq n_b \leq N_b = 96$. Following previous works,^{12,35} we quantified the main features of this final solution by computing the median across bootstrap solutions of means $\text{Med}_{(n_b)}(E[\chi]_{n_b})$, variances $\text{Med}_{(n_b)}(V[\chi]_{n_b})$ and covariances $\text{Med}_{(n_b)}(C[\chi, \chi']_{n_b})$ of the per-bootstrap isotropic diffusivity, squared normalized anisotropy, and longitudinal relaxation rate $\chi, \chi' = D_{\text{iso}}, D_{\Delta}^2, R_1$, respectively. Here, the median operator $\text{Med}_{(n_b)}(\cdot)$ acts across bootstrap solutions and $E[\cdot]_{n_b}$, $V[\cdot]_{n_b}$ and $C[\cdot, \cdot]_{n_b}$ denote the per-bootstrap average, variance and covariance over the diffusion-relaxation components forming the bootstrap solution n_b , respectively. For simplicity, we omit the explicit mention of the median operator when addressing a statistical descriptor, thereby writing averages, variances and covariances as $E[\chi]$, $V[\chi]$ and $C[\chi, \chi']$ respectively.

By design, the Monte-Carlo inversion algorithm progressively builds up the sought-for intra-voxel distribution $\mathcal{P}(\mathbf{D}, R_1)$ as a non-parametric discrete weighted sum of components. This implies that tissue-specific statistical descriptors can be extracted by subdividing the 5D configuration space of $\mathcal{P}(\mathbf{D}, R_1)$ into multiple bins. For instance, the "thin", "thick" and "big" bins introduced in Refs. 12 and 59 aim to isolate the signal contributions from white matter, grey matter and cerebrospinal fluid,

respectively. In this work, the boundaries of these bins, illustrated in the panels C, D and E of Figure 2, were defined as follows:

- "big" bin within $D_{\text{iso}} \in [2, 10] \mu\text{m}^2/\text{ms}$, $D_{\parallel}/D_{\perp} \in [0.01, 1000]$ and $R_1 \in [0.01, 10] \text{s}^{-1}$.
- "thick" bin within $D_{\text{iso}} \in [0.1, 2] \mu\text{m}^2/\text{ms}$, $D_{\parallel}/D_{\perp} \in [0.01, 4]$ and $R_1 \in [0.01, 10] \text{s}^{-1}$.
- "thin" bin within $D_{\text{iso}} \in [0.1, 2] \mu\text{m}^2/\text{ms}$, $D_{\parallel}/D_{\perp} \in [4, 1000]$ and $R_1 \in [0.01, 10] \text{s}^{-1}$.

As such, the "big" bin captures highly diffusive components, the "thick" bin captures components that are not highly diffusive nor highly anisotropic, and the "thin" bin captures components that are highly anisotropic. Note that the above bin boundaries extend far beyond the inversion boundaries listed in Section II B 1, so that to produce aesthetically pleasing figures such as the panels C, D and E of Figure 2. Bin-specific statistical descriptors were estimated following the aforementioned process for the retrieved components that specifically fall into each bin.

3. Orientation distribution functions (ODFs)

Orientation distribution functions (ODFs) can be defined from the thin-bin components output by the Monte-Carlo signal inversion of Section II B 1 using the procedure detailed in Refs. 71 and 72. Briefly, per-bootstrap ODFs were generated by convolving the discrete ensemble of weights w_i and unit-orientations (θ_i, ϕ_i) of the components belonging to the thin bin in each bootstrap solution n_b , $\{(w_i, \theta_i, \phi_i)\}_{n_b, i \in \{\text{thin bin}\}}$, with a Watson kernel. The purpose of this kernel is to smoothly map the discrete set of components onto the nearest nodes of a dense spherical mesh $\{(\theta_{\text{mesh}}, \phi_{\text{mesh}})\}$. A final voxel-wise ODF $P(\theta_{\text{mesh}}, \phi_{\text{mesh}})$ was calculated as the median of the per-bootstrap ODFs. In this work, we considered a 1000-point uniform spherical mesh and set the concentration parameter of the Watson kernel to $\kappa = 14.9$, following the rationale detailed in Ref. 71.

Following a similar procedure, the discrete set of diffusion-relaxation metrics $\{(D_{\parallel, i}, D_{\perp, i}, R_{1, i})\}_{n_b, i \in \{\text{thin bin}\}}$ can also be mapped onto this spherical mesh,^{71,72} yielding the orientation-specific diffusion-relaxation measures $\hat{E}[\chi]_{n_b}(\theta_{\text{mesh}}, \phi_{\text{mesh}})$, with $\chi \equiv D_{\text{iso}}, D_{\Delta}^2, R_1$. In addition to coloring ODFs according to the $(\theta_{\text{mesh}}, \phi_{\text{mesh}})$ local orientation, this mapping allows to color ODFs according to the local value $\text{Med}_{(n_b)}(\hat{E}[\chi]_{n_b}(\theta_{\text{mesh}}, \phi_{\text{mesh}}))$, thereby improving the visualization of orientation-specific diffusion-relaxation quantities. For simplicity, the short-hand notation " $\hat{E}[\chi]$ " is now retained instead for $\text{Med}_{(n_b)}(\hat{E}[\chi]_{n_b}(\theta_{\text{mesh}}, \phi_{\text{mesh}}))$.

C. Monte-Carlo density-peak clustering (MC-DPC)

The Monte-Carlo signal inversion algorithm of Section II B 1 can be combined with density-peak clustering (DPC)¹⁰⁸ according to the work presented in Ref. 73. This combination, called "Monte-Carlo density-peak clustering" (MC-DPC), enables to quantify the median value and precision of orientation-resolved means of $\chi = D_{\text{iso}}, D_{\Delta}^2, R_1, T_1 = 1/R_1$ across bootstrap solutions. We used MC-DPC to detect statistically significant differences between sub-voxel fiber populations robustly assigned to major fiber bundles *a posteriori*.

Firstly, MC-DPC gathers the ensemble $\{\mathcal{E}_{n_b}^{\text{thin}}\}_{1 \leq n_b \leq N_b}$ of all per-bootstrap thin-bin solution sets $\mathcal{E}_{n_b}^{\text{thin}} = \{(D_{\parallel, i}, D_{\perp, i}, \theta_i, \phi_i, R_{1, i}, w_i)\}_{n_b, i \in \{\text{thin bin}\}}$ and delineates N_c clusters in its orientation subspace using DPC with data-point density and outlier detection altered to account for the weights w_i of the retrieved thin-bin components.⁷³ An initial number of clusters N_c is automatically set by the number of voxel-wise ODF peaks, but may be reduced by MC-DPC following a filtering approach detailed in Ref. 73. Assuming that the estimated clusters, resulting from orientational aggregates of the all-bootstrap thin-bin solutions, can be interpreted as orientational regions of interest associated with sub-voxel fiber populations, MC-DPC then computes orientation-resolved statistics across bootstrap solutions. To do so, it separately classifies each per-bootstrap ensemble of thin-bin solutions $\mathcal{E}_{n_b}^{\text{thin}}$ into N_c ensembles $\mathcal{E}_{n_b, n_c}^{\text{thin}}$ (with $1 \leq n_c \leq N_c$), each containing the thin-bin solutions of bootstrap solution n_b that belong to an estimated cluster n_c . It then averages the properties of the solutions within each ensemble $\mathcal{E}_{n_b, n_c}^{\text{thin}}$ independently, yielding the orientation-resolved means

$$\hat{E}[\chi]_{n_b, n_c} = \frac{\sum_{k \in \mathcal{E}_{n_b, n_c}^{\text{thin}}} w_k \chi_k}{\sum_{k \in \mathcal{E}_{n_b, n_c}^{\text{thin}}} w_k}, \quad (4)$$

with $\chi \equiv x, y, z, D_{\text{iso}}, D_{\Delta}^2, R_1, T_1 = 1/R_1$, where (x, y, z) are the Cartesian coordinates of a component's orientation (θ, ϕ) . The short-hand notation " $\hat{E}[\chi]$ " will be used for simplicity to describe the collection of orientation-resolved means $\hat{E}[\chi]_{n_b, n_c}$ originating from all bootstrap solutions n_b and all clusters n_c . The orientation-resolved means of T_1 and R_1 in Equation 4 are computed separately, as both quantities are commonly found in the MRI literature and $\hat{E}[T_1]$ does not equal $1/\hat{E}[R_1]$. Finally, we extracted the median and interquartile range of our various orientation-resolved means $\hat{E}[\chi]$ across bootstrap solutions.

Non-parametric Mann-Whitney U -tests were used to assess whether or not two orientation-resolved means $\hat{E}[\chi]$ characterizing distinct white-matter fiber bundles are sampled from identically shaped non-median-shifted continuous distributions (null hypothesis \mathcal{H}_0). The p -values resulting from these tests inform on the acceptance or rejection of \mathcal{H}_0 at a certain significance level. In

particular, rejections of \mathcal{H}_0 at $p < 0.01$, $0.01 \leq p < 0.05$ and $0.05 \leq p < 0.1$ were used as proxies for detecting significant differences between two bundles with respect to a given type of orientation-resolved mean.

III. RESULTS

Figure 2 presents the fitted signals and the intra-voxel distributions $\mathcal{P}(\mathbf{D}, R_1)$ estimated by the Monte-Carlo signal inversion algorithm of Section II B 1 in typical voxels associated with cerebrospinal fluid (CSF) in the ventricles, cortical grey matter (GM) and white matter (WM) in the corpus callosum. Figure 3 displays typical axial maps of the statistical descriptors and bin-specific statistical descriptors described in Section II B 2. Figure 4 shows orientation-colored and $\hat{E}[R_1]$ -colored ODFs (see Section II B 3) in a typical axial slice. Figures 5 and 6 investigate possible microstructural differences between sub-voxel fiber populations leveraging MC-DPC (see Section II C) in regions of interest that target specific fiber crossings. While Figure 5 focuses on the crossing between the corpus callosum (CC) and the cingulum (CING), Figure 6 focuses on the crossing between the corpus callosum (CC), the arcuate fasciculus (AF) and the corticospinal tract (CST) in the posterior corona radiata.

IV. DISCUSSION

Figure 2 demonstrates that the Monte-Carlo signal inversion algorithm described in Section II B 1 adequately fits the measured signal in various voxels pertaining to WM, cortical GM and CSF in the ventricles. Additionally, the bins defined in Section II B 2 appear to capture these environments in accordance with their original design, *i.e.* the thin, thick and big bins capture components typically associated with WM, GM and CSF, respectively.

Figure 3 shows that the Monte-Carlo signal inversion algorithm can estimate maps of $\mathcal{P}(\mathbf{D}, R_1)$'s statistical descriptors. In particular, it retrieves maps that are consistent with those thoroughly discussed in Ref. 12, namely the S_0 , $E[D_{\text{iso}}]$, $E[D_{\Delta}^2]$, $V[D_{\text{iso}}]$, $V[D_{\Delta}^2]$ and $C[D_{\text{iso}}, D_{\Delta}^2]$ maps, along with the bin-specific $E[D_{\text{iso}}]$, $E[D_{\Delta}^2]$ and average local orientation $E[(\theta, \phi)]$ maps, and the bin-segmentation map. Let us thus mainly discuss the R_1 -related maps. The $E[R_1]$ map resembles an expected low-resolution T_1 map, *i.e.* bright in WM, slightly darker in GM and very dark in CSF. The $V[R_1]$ map resembles a noisier version of the $V[D_{\text{iso}}]$ map, as both give high values in mixed CSF-WM/GM voxels. The noise in $V[R_1]$ could be reduced upon adding more repetition times in the acquisition scheme. The $C[D_{\text{iso}}, R_1]$ map is negative at the interface between CSF and either WM or cortical GM. Indeed, upon entering CSF from WM/GM, D_{iso} increases rapidly and T_1 relaxation slows down (rapidly decreasing R_1). Finally, the $C[D_{\Delta}^2, R_1]$ map exhibits no

specific pattern. As for the bin-specific $E[R_1]$ maps, they present a clear contrast between our tissue-specific bins, due to a fast T_1 relaxation in WM, a slower relaxation in GM and an even slower relaxation in CSF.

Figure 4 features non-parametric ODFs capturing local orientations that are consistent with the known anatomy. Regarding $\hat{E}[R_1]$ -colored ODFs (see Section II B 3), they appear to change colors when approaching tissue interfaces with CSF. This gradual change in $\hat{E}[R_1]$ may originate from exchange between tissues and CSF in these regions. Importantly, Figure 4 shows that potential differences in T_1 relaxation may exist between major fiber bundles, namely CC and CING (insets in Figure 4), and CC, AF and CST (as indicated by greener $\hat{E}[R_1]$ -colored ODFs where the CST's pyramidal tracts are located).

These potential microstructural differences are quantified in Figures 5 and 6. Let us focus on relaxation-based differences. Figure 5 shows that CC and CING exhibit significant differences in $\hat{E}[R_1]$ that are qualitatively consistent with those found in Refs. 7 and 32, *i.e.* R_1 tends to be lower in CING compared to CC. As for Figure 6, it shows that CST features significant differences in $\hat{E}[R_1]$ and $\hat{E}[T_1]$ with CC and AF (but no statistically significant differences between CC and AF). These differences are qualitatively consistent with those identified for CST in Ref. 7, *i.e.* T_1 tends to be higher in CST compared to CC and AF.

Quantitatively, the T_1 values estimated by $\hat{E}[T_1]$ in Figures 5 and 6 (around 1.5 to 2 seconds) are overestimated compared to those of Ref. 7 (around 0.9 to 1 second) and Ref. 32 (around 0.7 second). This discrepancy can be explained by either or both of the following factors. Firstly, the acquisition scheme described in Section II A does not maximize the amount of diffusion-relaxation correlations built into the inversion kernel of Equation 1, because the same diffusion-weighting block was repeated for each acquired repetition time. Similar problems have been suggested to lead to a loss of accuracy for the Monte-Carlo signal inversion.³⁵ Second, the use of saturation recovery with a spoiled spin echo for T_1 encoding is very sensitive to flip-angle inaccuracies caused by both B_1^+ inhomogeneity across the subject and slice profile imperfections. Saturation-recovery based T_1 mapping is also sensitive to magnetization-transfer effects, especially in the present setup comprising an additional refocusing pulse as well as a fat-saturation pulse.^{109–111} These technical limitations should be mitigated upon developing a sequence that includes inversion preparation for enhanced T_1 sensitivity and slice shuffling for optimized time efficiency.^{8,9}

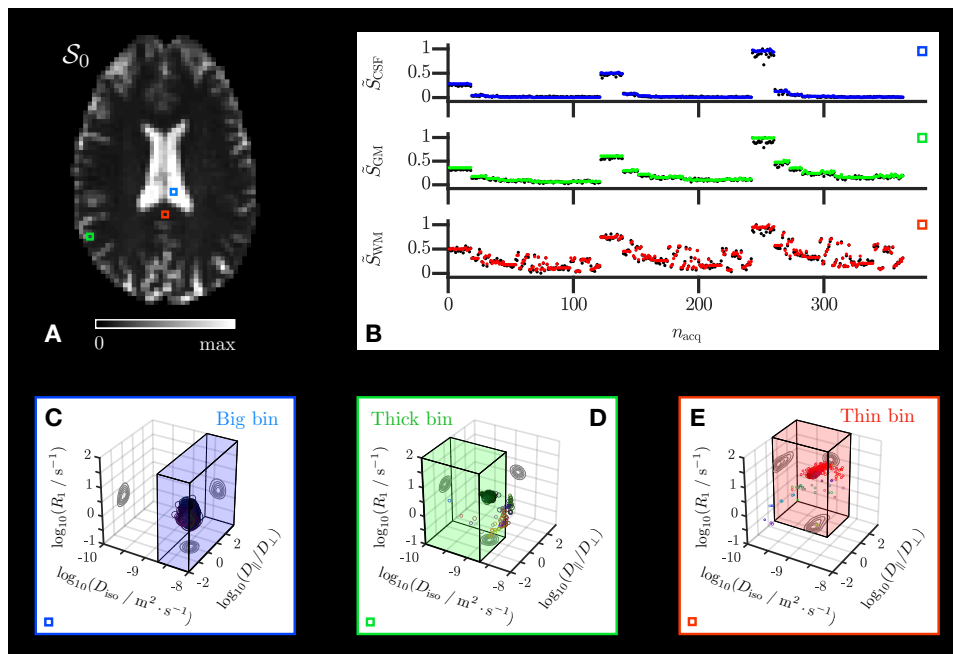


Figure 2. Monte-Carlo fitted signal and retrieved 5D distributions $\mathcal{P}(\mathbf{D}, R_1)$ in typical voxels. (A) \mathcal{S}_0 map estimated by the Monte-Carlo inversion. The colored squares delineate typical CSF (blue), GM (green) and WM (red) voxels. (B) Normalized signal $\tilde{S} = S/\max(S)$ measured (black points) and fitted (colored points) in the archetypal voxels of panel A as a function of the sorted acquisition point index n_{acq} of Figure 1. (C,D,E) Non-parametric distributions $\mathcal{P}(\mathbf{D}, R_1)$ estimated within the archetypal voxels of panel A and reported as scatter plots in a 3D space of the logarithms of the longitudinal relaxation rate R_1 , isotropic diffusivity D_{iso} , and axial-radial diffusivity ratio D_{\parallel}/D_{\perp} . Diffusion-orientations (θ, ϕ) are color-coded according to $[\text{red}, \text{green}, \text{blue}] = [\sin \theta \cos \phi, \sin \theta \sin \phi, \cos \theta] \times |D_{\parallel} - D_{\perp}|/\max(D_{\parallel}, D_{\perp})$. Symbol area is proportional to the statistical weight w_n/S_0 of the corresponding component n . The contour lines on the sides of the plots represent projections of the 5D distributions $\mathcal{P}(\mathbf{D}, R_1)$ onto the respective 2D planes. The "thin", "thick" and "big" bins defined in Section II B 2 are illustrated in the panels where they are most relevant.

V. CONCLUSIONS

Diffusion- T_1 weighted datasets incorporating multiple b-tensor shapes can be inverted to obtain non-parametric distributions $\mathcal{P}(\mathbf{D}, R_1)$ of diffusion tensors and longitudinal relaxation rates using the Monte-Carlo signal inversion algorithm. The main features of the retrieved distributions can be visualized as maps and bin-specific maps of statistical descriptors related to means, variances and covariances of diffusion-relaxation properties. In particular, the bin-specific $E[R_1]$ maps exhibit the expected R_1 contrast between white matter, grey matter and CSF. Further insight into white-matter microstructure is provided by the "thin bin", which isolates highly anisotropic components that should report on white-matter tissues. From these thin-bin components, visualization of fiber-specific information is improved upon defining orientation distribution functions (ODFs) that can be color-mapped with respect to local orientation or diffusion-relaxation features.⁷¹ While $\hat{E}[R_1]$ -colored ODFs hint at possible differences between fiber bundles, Monte-Carlo density-peak clustering (MC-DPC) enables their quantification in terms of fiber-specific diffusion-relaxation measures.⁷³

Importantly, significant differences with respect to longitudinal relaxation are detected between the corpus callosum and the cingulum, and between the corticospinal tract and the corpus callosum and arcuate fasciculus. These differences, qualitatively consistent with those found in previous works,^{7,32} offer a proof of concept for the potential of our Monte-Carlo framework in terms of non-parametric fiber-specific T_1 relaxometry. Such approach would be practical in identifying differences in T_1 between distinct sub-voxel fiber populations, characterizing developmental or pathological changes in T_1 within a given sub-voxel fiber population, and measuring the angular dependence of longitudinal relaxation times in white matter with respect to the main MRI magnetic field \mathbf{B}_0 .^{112,113} Moreover, non-parametric fiber-specific T_1 relaxometry would be highly relevant to microstructure-informed tractography.¹¹⁴⁻¹¹⁶

Nevertheless, our work can still be improved in two main ways. Firstly, the acquisition scheme could be optimized in terms of speed^{8,9} and sensitivity.¹¹⁷⁻¹¹⁹ Second, MC-DPC could be combined with tractography to better assign MC-DPC's output clusters to their corresponding fiber bundles. These ideas will be explored in future investigations.

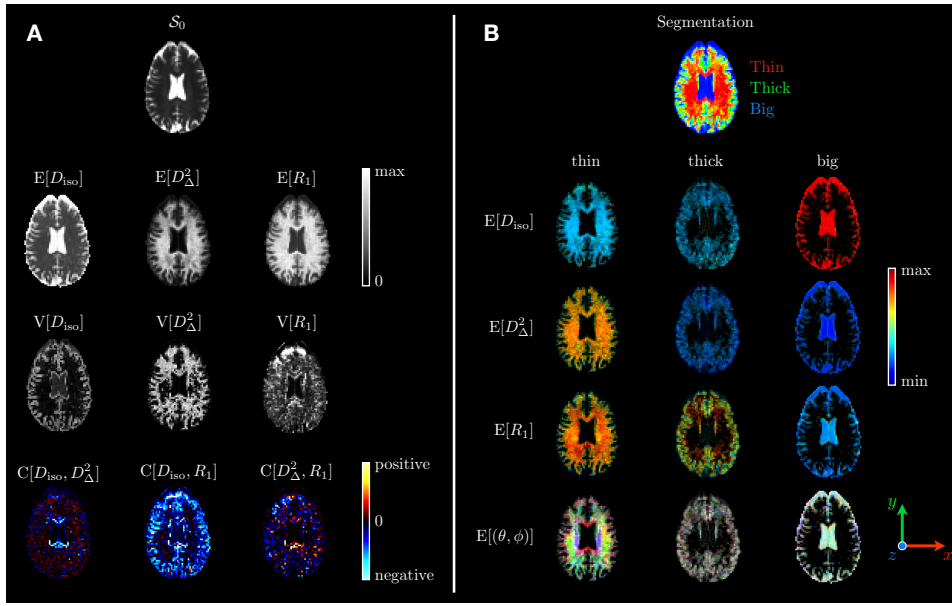


Figure 3. Typical axial maps of the statistical descriptors described in Section II B 2. The various colormaps are bounded by the following values: $S_0 \in [0, \max(S_0)]$, $E[D_{\text{iso}}] \in [0, 3.5] \mu\text{m}^2/\text{ms}$, $E[D_{\Delta}^2] \in [0, 1]$, $E[R_1] \in [0, 0.8] \text{s}^{-1}$, $V[D_{\text{iso}}] \in [0, 0.9] \mu\text{m}^4/\text{ms}^2$, $V[D_{\Delta}^2] \in [0, 0.1]$, $V[R_1] \in [0, 0.13] \text{s}^{-2}$, $C[D_{\text{iso}}, D_{\Delta}^2] \in [-0.3, 0.3] \mu\text{m}^2/\text{ms}$, $C[D_{\text{iso}}, R_1] \in [-2.4, 2.4] \times 10^{-4} \mu\text{m}^2/\text{ms}^2$ and $C[D_{\Delta}^2, R_1] \in [-0.08, 0.08] \text{s}^{-1}$. The bin-specific average intra-voxel orientation $E[(\theta, \phi)]$ is color-coded for orientation according to $[\text{red}, \text{green}, \text{blue}] = [E[D_{xx}], E[D_{yy}], E[D_{zz}]]/\max(E[D_{xx}], E[D_{yy}], E[D_{zz}])$, where the average diffusivities $E[D_{ii}]$ are associated with the directions $i = x, y, z$ corresponding to the "left-right", "anterior-posterior" and "superior-inferior" directions, respectively. For a given bin, the intensity of the bin-specific maps equals the voxel-wise average fraction f_{bin} of components belonging to this bin. The segmentation map is colored according to $[\text{red}, \text{green}, \text{blue}] = [f_{\text{thin}}, f_{\text{thick}}, f_{\text{big}}]/\max(f_{\text{thin}}, f_{\text{thick}}, f_{\text{big}})$.

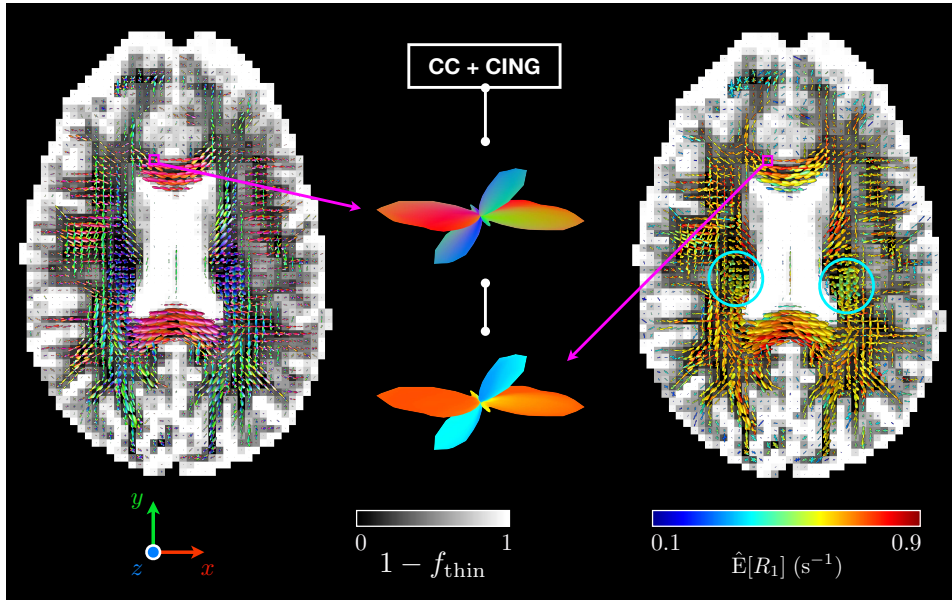


Figure 4. Axial greyscale maps of the fraction of non thin-bin components $1 - f_{\text{thin}}$ with superimposed ODFs colored by local orientation (with x , y and z corresponding to the "left-right", "anterior-posterior" and "superior-inferior" directions, respectively) and by $\hat{E}[R_1]$ (see Section II B 3). The middle insets zoom on a voxel containing a fiber crossing between the corpus callosum (CC) and the cingulum (CING), and presents the estimated orientation-colored and $\hat{E}[R_1]$ -colored ODFs for this voxel. While differences in $\hat{E}[R_1]$ seem to exist between CC and CING, such differences may also exist in the regions where the CST's pyramidal tracts are located (blue circles), as indicated by the greener $\hat{E}[R_1]$ -colored ODFs therein.

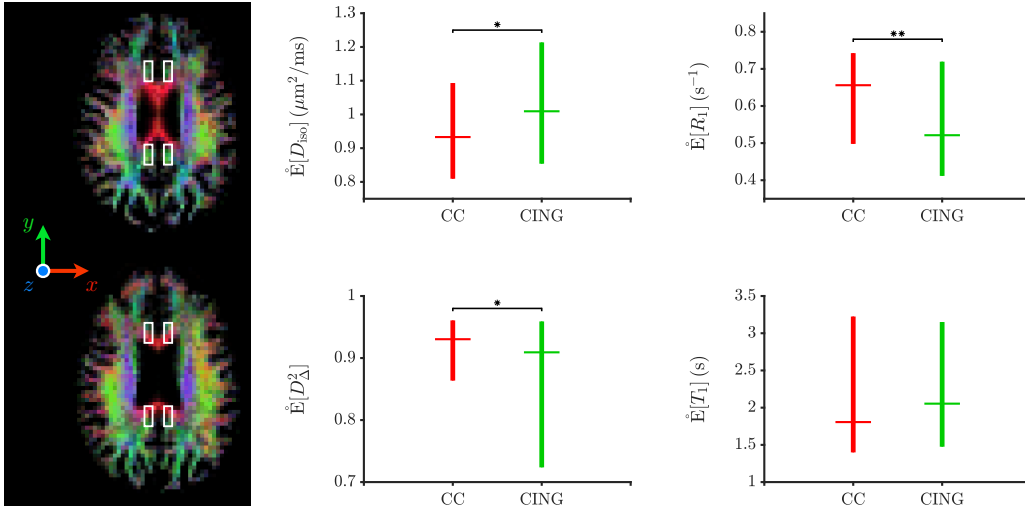


Figure 5. Boxplots of the medians of the orientation-resolved means $\dot{E}[\chi]$ obtained from MC-DPC (see Equation 4) within the regions of interest drawn in the left panel (white-lined boxes), showing two axial slices of the orientation-colored average fraction of thin-bin components f_{thin} . For a given boxplot, the horizontal line and whiskers indicate the median and the range between the first and third quartiles of the medians of the orientation-resolved means $\dot{E}[\chi]$, respectively. The chosen regions of interest focus on crossing areas between the corpus callosum (CC) and the cingulum (CING). Each MC-DPC cluster (and associated orientation-resolved means) is robustly assigned to one of these bundles depending on whether its median orientation is closer to the x "left-right" direction (CC) or to the y "anterior-posterior" direction (CING). The asterisks report the results of non-parametric Mann-Whitney U -tests assessing whether or not two orientation-resolved means $\dot{E}[\chi]$ assigned to distinct bundles are sampled from identically shaped non-median-shifted continuous distributions (null hypothesis \mathcal{H}_0). The p -values resulting from these tests inform on the acceptance or rejection of \mathcal{H}_0 at a certain significance level: $0.05 \leq p < 0.1$ (*) and $0.01 \leq p < 0.05$ (**).

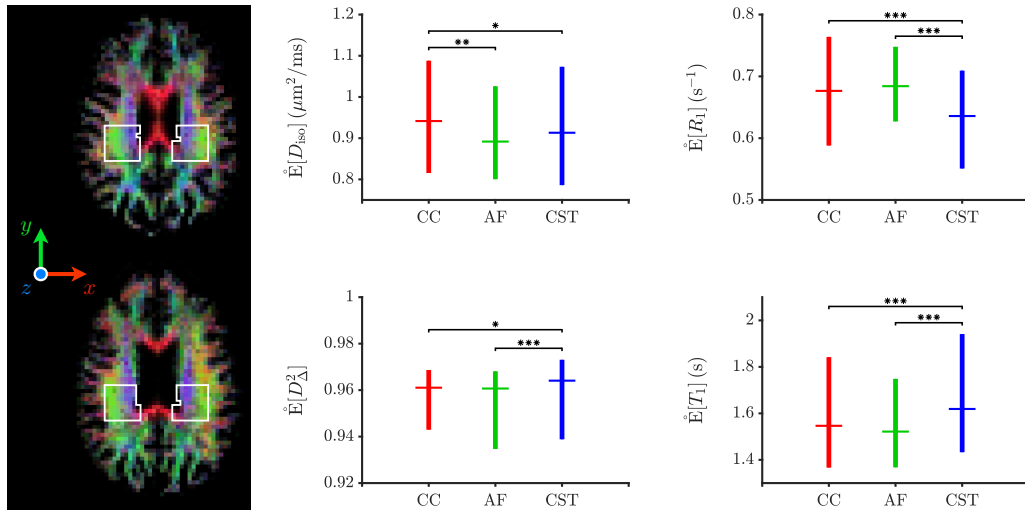


Figure 6. Equivalent of Figure 5 for regions of interest focusing on crossing areas between the corpus callosum (CC), the arcuate fasciculus (AF) and the corticospinal tract (CST) in the posterior corona radiata. Each MC-DPC cluster (and associated orientation-resolved means) is robustly assigned to one of these bundles depending on whether its median orientation is closer to the x "left-right" direction (CC), to the y "anterior-posterior" direction (AF), or to the z "superior-inferior" direction (CST). The asterisks report the results of non-parametric Mann-Whitney U -tests assessing whether or not two orientation-resolved means $\dot{E}[\chi]$ assigned to distinct bundles are sampled from identically shaped non-median-shifted continuous distributions (null hypothesis \mathcal{H}_0). The p -values resulting from these tests inform on the acceptance or rejection of \mathcal{H}_0 at a certain significance level: $0.05 \leq p < 0.1$ (*), $0.01 \leq p < 0.05$ (**), and $p < 0.01$ (***)

ACKNOWLEDGMENTS

This work was financially supported by the Swedish Foundation for Strategic Research (ITM17-0267) and the

Swedish Research Council (2018-03697). D. Topgaard owns shares in Random Walk Imaging AB (Lund, Sweden, <http://www.rwi.se/>), holding patents related to the described methods.

- * alexis.reymbaut@fkem1.lu.se
- ¹ D. Le Bihan, *Radiology* **177**, 328 (1990), pMID: 2217762.
 - ² D. Le Bihan, R. Turner, P. Douek, and N. Patronas, *American Journal of Roentgenology* **159**, 591 (1992).
 - ³ P. J. Basser, J. Mattiello, and D. LeBihan, *Biophys J* **66**, 259 (1994).
 - ⁴ D. K. Jones, *Diffusion MRI* (Oxford University Press, 2010).
 - ⁵ Y. Zhang and B. Blümich, *Journal of magnetic resonance (San Diego, Calif. : 1997)* **242**, 41–48 (2014).
 - ⁶ S. De Santis, D. Barazany, D. K. Jones, and Y. Assaf, *Magnetic Resonance in Medicine* **75**, 372 (2016).
 - ⁷ S. de Santis, Y. Assaf, B. Jeurissen, D. K. Jones, and A. Roebroeck, *NeuroImage* **141**, 133 (2016).
 - ⁸ J. Hutter, P. J. Sator, D. Christiaens, R. P. A. G. Teixeira, T. Roberts, L. Jackson, A. N. Price, S. Malik, and J. V. Hajnal, *Scientific Reports* **8**, 15138 (2018).
 - ⁹ D. J. Park, T. Witzel, I. Leppert, Y.-F. Yen, Q. Fan, C. Tardif, and J. Polimeni (International Society for Magnetic Resonance Imaging (ISMRM), 2018).
 - ¹⁰ P. J. Sator, J. Hutter, M. Palombo, L. H. Jackson, A. Ho, E. Panagiotaki, L. C. Chappell, M. A. Rutherford, J. V. Hajnal, and D. C. Alexander, *Magnetic Resonance in Medicine* **82**, 95 (2019).
 - ¹¹ J. P. de Almeida Martins and D. Topgaard, *Scientific Reports* **8**, 2488 (2018).
 - ¹² J. P. de Almeida Martins, C. M. W. Tax, F. Szczepankiewicz, D. K. Jones, C.-F. Westin, and D. Topgaard, *Magnetic Resonance* **1**, 27 (2020).
 - ¹³ N. BLOEMBERGEN, E. M. PURCELL, and R. V. POUND, *Nature* **160**, 475 (1947).
 - ¹⁴ N. Bloembergen, E. M. Purcell, and R. V. Pound, *Phys. Rev.* **73**, 679 (1948).
 - ¹⁵ H. T. EDZES and E. T. SAMULSKI, *Nature* **265**, 521 (1977).
 - ¹⁶ B. Halle, *Magnetic Resonance in Medicine* **56**, 60 (2006).
 - ¹⁷ W. D. Rooney, G. Johnson, X. Li, E. R. Cohen, S.-G. Kim, K. Ugurbil, and C. S. Springer Jr., *Magnetic Resonance in Medicine* **57**, 308 (2007).
 - ¹⁸ J. P. Mottershead, K. Schmierer, M. Clemence, J. S. Thornton, F. Scaravilli, G. J. Barker, P. S. Tofts, J. Newcombe, M. L. Cuzner, R. J. Ordidge, W. I. McDonald, and D. H. Miller, *Journal of Neurology* **250**, 1293 (2003).
 - ¹⁹ T. Bjarnason, I. Vavasour, C. Chia, and A. MacKay, *Magnetic Resonance in Medicine* **54**, 1072 (2005).
 - ²⁰ S. D. Santis], M. Drakesmith, S. Bells, Y. Assaf, and D. K. Jones, *NeuroImage* **89**, 35 (2014).
 - ²¹ A. Lutti, F. Dick, M. I. Sereno, and N. Weiskopf, *NeuroImage* **93**, 176 (2014), in-vivo Brodmann Mapping of the Human Brain.
 - ²² C. Stüber, M. Morawski, A. Schäfer, C. Labadie, M. Wähner, C. Leuze, M. Streicher, N. Barapatre, K. Reimann, S. Geyer, D. Spemann, and R. Turner, *NeuroImage* **93**, 95 (2014).
 - ²³ K. Brownstein and C. Tarr, *Journal of Magnetic Resonance (1969)* **26**, 17 (1977).
 - ²⁴ G. J. Stanisz, G. A. Wright, R. M. Henkelman, and A. Szafer, *Magnetic Resonance in Medicine* **37**, 103 (1997).
 - ²⁵ D. G. Norris, *NMR in Biomedicine* **14**, 77 (2001).
 - ²⁶ J. V. Sehy, J. J. Ackerman, and J. J. Neil, *Magnetic Resonance in Medicine* **48**, 765 (2002).
 - ²⁷ L. Minati and W. P. Weglarz, *Concepts in Magnetic Resonance Part A* **30A**, 278 (2007).
 - ²⁸ R. V. Mulkern, S. J. Haker, and S. E. Maier, *Magn Reson Imaging* **27**, 1151 (2009), 19520535[pmid].
 - ²⁹ J. Veraart, D. S. Novikov, and E. Fieremans, *NeuroImage* **182**, 360 (2018), microstructural Imaging.
 - ³⁰ G. Lemberskiy, E. Fieremans, J. Veraart, F.-M. Deng, A. B. Rosenkrantz, and D. S. Novikov, *Frontiers in Physics* **6**, 91 (2018).
 - ³¹ L. Ning, B. Gagoski, F. Szczepankiewicz, C. Westin, and Y. Rathi, *IEEE Transactions on Medical Imaging* **39**, 668 (2020).
 - ³² D. A. Andrews, J. S. W. Campbell, I. R. Leppert, D. J. Park, G. B. Pike, J. R. Polimeni, and C. L. Tardif (International Society for Magnetic Resonance Imaging (ISMRM), 2019).
 - ³³ I. O. Jelescu and M. D. Budde, *Frontiers in Physics* **5**, 61 (2017).
 - ³⁴ D. S. Novikov, V. G. Kiselev, and S. N. Jespersen, *Magnetic Resonance in Medicine* **79**, 3172 (2018).
 - ³⁵ A. Reymbaut, P. Mezzani, J. P. de Almeida Martins, and D. Topgaard, *NMR in Biomedicine* **n/a**, e4267 (2020), e4267 nbm.4267.
 - ³⁶ S. Eriksson, S. Lasič, and D. Topgaard, *Journal of Magnetic Resonance* **226**, 13 (2013).
 - ³⁷ C.-F. Westin, F. Szczepankiewicz, O. Pasternak, E. Özarslan, D. Topgaard, H. Knutsson, and M. Nilsson, in *Medical Image Computing and Computer-Assisted Intervention – MICCAI 2014*, edited by P. Golland, N. Hata, C. Barillot, J. Hornegger, and R. Howe, MICCAI (Springer International Publishing, Cham, 2014) pp. 209–216.
 - ³⁸ S. Eriksson, S. Lasič, M. Nilsson, C.-F. Westin, and D. Topgaard, *The Journal of Chemical Physics* **142**, 104201 (2015).
 - ³⁹ C.-F. Westin, H. Knutsson, O. Pasternak, F. Szczepankiewicz, E. özarslan, D. van Westen, C. Mattisson, M. Bogren, L. J. O'Donnell, M. Kubicki, D. Topgaard, and M. Nilsson, *NeuroImage* **135**, 345 (2016).
 - ⁴⁰ D. Topgaard, *Journal of Magnetic Resonance* **275**, 98 (2017).
 - ⁴¹ D. Topgaard, *Journal of Magnetic Resonance* **306**, 150 (2019).
 - ⁴² J. Mattiello, P. Basser, and D. Lebihan, *Journal of Magnetic Resonance, Series A* **108**, 131 (1994).

- ⁴³ J. Mattiello, P. J. Basser, and D. Le Bihan, *Magnetic Resonance in Medicine* **37**, 292 (1997).
- ⁴⁴ U. Haeberlen, *High resolution NMR in solids : selective averaging* (Academic Press, New York, 1976) p. v. .:
- ⁴⁵ T. E. Conturo, R. C. McKinstry, E. Akbudak, and B. H. Robinson, *Magnetic Resonance in Medicine* **35**, 399 (1996).
- ⁴⁶ S. Lasič, F. Szczepankiewicz, S. Eriksson, M. Nilsson, and D. Topgaard, *Frontiers in Physics* **2**, 11 (2014).
- ⁴⁷ M. Cottaar, F. Szczepankiewicz, M. Bastiani, M. Hernandez-Fernandez, S. N. Sotiropoulos, M. Nilsson, and S. Jbabdi, *NeuroImage*, 116832 (2020).
- ⁴⁸ B. Lampinen, F. Szczepankiewicz, J. Mårtensson, D. van Westen, P. C. Sundgren, and M. Nilsson, *NeuroImage* **147**, 517 (2017).
- ⁴⁹ S. Coelho, J. M. Pozo, S. N. Jespersen, D. K. Jones, and A. F. Frangi, *Magnetic Resonance in Medicine* **82**, 395 (2019).
- ⁵⁰ S. Coelho, J. M. Pozo, S. N. Jespersen, and A. F. Frangi, *Medical Image Computing and Computer Assisted Intervention – MICCAI 2019* (Springer International Publishing, Cham, 2019) pp. 617–625.
- ⁵¹ M. Reisert, V. G. Kiselev, and B. Dhital, *Magnetic Resonance in Medicine* **81**, 3819 (2019).
- ⁵² B. Lampinen, F. Szczepankiewicz, J. Mårtensson, D. van Westen, O. Hansson, C.-F. Westin, and M. Nilsson, *Magnetic Resonance in Medicine* **00**, 1 (2020).
- ⁵³ A. Reymbaut, A. Valcourt Caron, G. Gilbert, F. Szczepankiewicz, M. Nilsson, S. K. Warfield, M. Descoteaux, and B. Scherrer, *arXiv e-prints* (2020), [arXiv:2004.07340 \[physics.med-ph\]](https://arxiv.org/abs/2004.07340).
- ⁵⁴ M. Prange and Y.-Q. Song, *Journal of Magnetic Resonance* **196**, 54 (2009).
- ⁵⁵ P. Galvosas and P. T. Callaghan, *Comptes Rendus Physique* **11**, 172 (2010), multiscale NMR and relaxation.
- ⁵⁶ D. Bernin and D. Topgaard, *Current Opinion in Colloid and Interface Science* **18**, 166 (2013).
- ⁵⁷ Y.-Q. Song, L. Venkataramanan, R. Kausik, and N. Heaton, in *Diffusion NMR of Confined Systems: Fluid Transport in Porous Solids and Heterogeneous Materials* (The Royal Society of Chemistry, 2017) pp. 111–155.
- ⁵⁸ J. P. de Almeida Martins and D. Topgaard, *Phys. Rev. Lett.* **116**, 087601 (2016).
- ⁵⁹ D. Topgaard, *NMR in Biomedicine* **32**, e4066 (2019).
- ⁶⁰ L. Venkataramanan, Yi-Qiao Song, and M. D. Hurlmann, *IEEE Transactions on Signal Processing* **50**, 1017 (2002).
- ⁶¹ D. Benjamini and P. J. Basser, *Journal of Magnetic Resonance* **271**, 40 (2016).
- ⁶² D. Kim, E. K. Doyle, J. L. Wisnowski, J. H. Kim, and J. P. Haldar, *Magnetic Resonance in Medicine* **78**, 2236 (2017).
- ⁶³ D. Benjamini and P. J. Basser, *Microporous and Mesoporous Materials* **269**, 93 (2018), proceedings of the 13th International Bologna Conference on Magnetic Resonance in Porous Media (MRPM13).
- ⁶⁴ D. Benjamini and P. J. Basser, *NMR in Biomedicine* **n/a**, e4226 (2020).
- ⁶⁵ D. Kim, J. L. Wisnowski, C. T. Nguyen, and J. P. Haldar, *NMR in Biomedicine* **n/a**, e4244 (2020).
- ⁶⁶ S. W. Provencher, *Computer Physics Communications* **27**, 213 (1982).
- ⁶⁷ R. M. Kroeker and R. M. Henkelman, *Journal of Magnetic Resonance* (1969) **69**, 218 (1986).
- ⁶⁸ K. P. Whittall and A. L. MacKay, *Journal of Magnetic Resonance* (1969) **84**, 134 (1989).
- ⁶⁹ J. Mitchell, T. Chandrasekera, and L. Gladden, *Progress in Nuclear Magnetic Resonance Spectroscopy* **62**, 34 (2012).
- ⁷⁰ B. Jeurissen, A. Leemans, J.-D. Tournier, D. K. Jones, and J. Sijbers, *Human Brain Mapping* **34**, 2747 (2013).
- ⁷¹ J. P. de Almeida Martins, C. M. W. Tax, A. Reymbaut, F. Szczepankiewicz, D. K. Jones, and D. Topgaard, *bioRxiv* (2020), [10.1101/2020.05.23.111963](https://doi.org/10.1101/2020.05.23.111963).
- ⁷² J. P. de Almeida Martins, *Pushing diffusion MRI towards new dimensions*, *Ph.D. thesis*, Lund University, Lund University, Faculty of Science, Department of Chemistry, Division of Physical Chemistry (2020).
- ⁷³ A. Reymbaut, J. P. de Almeida Martins, C. M. W. Tax, F. Szczepankiewicz, D. K. Jones, and D. Topgaard, *arXiv e-prints* (2020), [arXiv:2004.08626 \[physics.med-ph\]](https://arxiv.org/abs/2004.08626).
- ⁷⁴ H. Liu, C. Rubino, A. V. Dvorak, M. Jarrett, E. Ljungberg, I. M. Vavasour, L. E. Lee, S. H. Kolind, E. L. MacMillan, A. Traboulsee, D. J. Lang, A. Rauscher, D. K. Li, A. L. MacKay, L. A. Boyd, J. L. Kramer, and C. Laule, *Journal of Neuroimaging* **29**, 699 (2019).
- ⁷⁵ M. P. van den Heuvel, R. C. W. Mandl, C. J. Stam, R. S. Kahn, and H. E. Hulshoff Pol, *Journal of Neuroscience* **30**, 15915 (2010).
- ⁷⁶ K. Caeyenberghs, C. Metzler-Baddeley, S. Foley, and D. K. Jones, *Journal of Neuroscience* **36**, 4056 (2016).
- ⁷⁷ M. Mancini, G. Giuliatti, N. Dowell, B. Spanò, N. Harrison, M. Bozzali, and M. Cercignani, *NeuroImage* **182**, 351 (2018), microstructural Imaging.
- ⁷⁸ C. Laule, I. M. Vavasour, S. H. Kolind, D. K. B. Li, T. L. Traboulsee, G. R. W. Moore, and A. L. MacKay, *Neurotherapeutics* **4**, 460 (2007).
- ⁷⁹ J. S. Campbell, I. R. Leppert, S. Narayanan, M. Boudreau, T. Duval, J. Cohen-Adad, G. B. Pike, and N. Stikov, *NeuroImage* **182**, 80 (2018), microstructural Imaging.
- ⁸⁰ A. Mackay, K. Whittall, J. Adler, D. Li, D. Paty, and D. Graeb, *Magnetic Resonance in Medicine* **31**, 673 (1994).
- ⁸¹ C. Beaulieu, F. R. Fenrich, and P. S. Allen, *Magnetic Resonance Imaging* **16**, 1201 (1998).
- ⁸² P. J. Gareau, B. K. Rutt, S. J. Karlik, and J. R. Mitchell, *Journal of Magnetic Resonance Imaging* **11**, 586 (2000).
- ⁸³ S. Webb, C. A. Munro, R. Midha, and G. J. Stanisz, *Magnetic Resonance in Medicine* **49**, 638 (2003).
- ⁸⁴ G. J. Stanisz, S. Webb, C. A. Munro, T. Pun, and R. Midha, *Magnetic Resonance in Medicine* **51**, 473 (2004).
- ⁸⁵ C. Laule, E. Leung, D. K. Li, A. L. Traboulsee, D. W. Paty, A. L. MacKay, and G. R. Moore, *Multiple Sclerosis Journal* **12**, 747 (2006).
- ⁸⁶ C. Laule, P. Kozlowski, E. Leung, D. K. Li, A. L. MacKay, and G. W. Moore, *NeuroImage* **40**, 1575 (2008).
- ⁸⁷ D. Hwang, D.-H. Kim, and Y. P. Du, *NeuroImage* **52**, 198 (2010).
- ⁸⁸ J. Lee, K. Shmueli, B.-T. Kang, B. Yao, M. Fukunaga, P. [van Gelderen], S. Palumbo, F. Bosetti, A. C. Silva, and J. H. Duyn, *NeuroImage* **59**, 3967 (2012).
- ⁸⁹ P. Sati, P. [van Gelderen], A. C. Silva, D. S. Reich, H. Merkle, J. A. [de Zwart], and J. H. Duyn, *NeuroImage* **77**, 268 (2013).
- ⁹⁰ K. Schmierer, C. A. Wheeler-Kingshott, D. J. Tozer, P. A. Boulby, H. G. Parkes, T. A. Yousry, F. Scaravilli, G. J.

- Barker, P. S. Tofts, and D. H. Miller, *Magnetic Resonance in Medicine* **59**, 268 (2008).
- ⁹¹ S. Mori, B. J. Crain, V. P. Chacko, and P. C. M. Van Zijl, *Annals of Neurology* **45**, 265 (1999).
- ⁹² P. J. Basser, S. Pajevic, C. Pierpaoli, J. Duda, and A. Aldroubi, *Magnetic Resonance in Medicine* **44**, 625 (2000).
- ⁹³ D. M. Morris, K. V. Embleton, and G. J. Parker, *NeuroImage* **42**, 1329 (2008).
- ⁹⁴ M. Reisert, I. Mader, C. Anastasopoulos, M. Weigel, S. Schnell, and V. Kiselev, *NeuroImage* **54**, 955 (2011).
- ⁹⁵ D. Christiaens, M. Reisert, T. Dhollander, S. Sunaert, P. Suetens, and F. Maes, *NeuroImage* **123**, 89 (2015).
- ⁹⁶ P. F. Neher, M.-A. Côté, J.-C. Houde, M. Descoteaux, and K. H. Maier-Hein, *NeuroImage* **158**, 417 (2017).
- ⁹⁷ L. Konopleva, K. A. Il'yasov, H. Skibbe, V. G. Kiselev, E. Kellner, B. Dhital, and M. Reisert, *NeuroImage* **174**, 576 (2018).
- ⁹⁸ P. Poulin, D. Jörgens, P.-M. Jodoin, and M. Descoteaux, *Magnetic Resonance Imaging* **64**, 37 (2019), artificial Intelligence in MRI.
- ⁹⁹ A. Haase, J. Frahm, W. Hanicke, and D. Matthaei, *Physics in Medicine and Biology* **30**, 341 (1985).
- ¹⁰⁰ F. Szczepankiewicz, J. Sjölund, F. Ståhlberg, J. Lätt, and M. Nilsson, *PLOS ONE* **14**, 1 (2019).
- ¹⁰¹ J. Sjölund, F. Szczepankiewicz, M. Nilsson, D. Topgaard, C.-F. Westin, and H. Knutsson, *Journal of Magnetic Resonance* **261**, 157 (2015).
- ¹⁰² F. Szczepankiewicz, C.-F. Westin, and M. Nilsson, *Magnetic Resonance in Medicine* **82**, 1424 (2019).
- ¹⁰³ H. Lundell, M. Nilsson, T. B. Dyrby, G. J. M. Parker, P. L. H. Cristinacce, F.-L. Zhou, D. Topgaard, and S. Lasič, *Scientific Reports* **9**, 9026 (2019).
- ¹⁰⁴ W. Perman, S. Hilal, H. Simon, and A. Maudsley, *Magnetic Resonance Imaging* **2**, 23 (1984), second Annual Meeting of the Society for Magnetic Resonance Imaging.
- ¹⁰⁵ C. L. Lawson and R. J. Hanson, *Solving least squares problems* (Society for Industrial and Applied Mathematics (SIAM), 1974).
- ¹⁰⁶ A. E. English, K. P. Whittall, M. L. G. Joy, and R. M. Henkelman, *Magnetic Resonance in Medicine* **22**, 425 (1991).
- ¹⁰⁷ D. W. de Kort, J. P. M. van Duynhoven, F. J. M. Hoeben, H. M. Janssen, and H. Van As, *Analytical Chemistry* **86**, 9229 (2014), PMID: 25141338.
- ¹⁰⁸ A. Rodriguez and A. Laio, *Science* **344**, 1492 (2014).
- ¹⁰⁹ S. D. Wolff and R. S. Balaban, *Magnetic Resonance in Medicine* **10**, 135 (1989).
- ¹¹⁰ R. P. A. G. Teixeira, S. J. Malik, and J. V. Hajnal, *Magnetic Resonance in Medicine* **81**, 907 (2019).
- ¹¹¹ R. P. A. G. Teixeira, R. Neji, T. C. Wood, A. A. Baburamani, S. J. Malik, and J. V. Hajnal, *Magnetic Resonance in Medicine* **84**, 221 (2020).
- ¹¹² R. M. Henkelman, G. J. Stanisiz, J. K. Kim, and M. J. Bronskill, *Magnetic Resonance in Medicine* **32**, 592 (1994).
- ¹¹³ M. J. Knight, R. A. Damion, and R. A. Kauppinen, *Biomedical spectroscopy and imaging* **7**, 125 (2018).
- ¹¹⁴ A. Daducci, A. Dal Palú, M. Descoteaux, and J.-P. Thiran, *Frontiers in Neuroscience* **10**, 247 (2016).
- ¹¹⁵ G. Girard, A. Daducci, L. Petit, J.-P. Thiran, K. Whittingstall, R. Deriche, D. Wassermann, and M. Descoteaux, *Human Brain Mapping* **38**, 5485 (2017).
- ¹¹⁶ M. Barakovic, *EPFL Thesis*, 165 (2019).
- ¹¹⁷ Y.-Q. Song, L. Venkataramanan, and L. Burcaw, *The Journal of Chemical Physics* **122**, 104104 (2005).
- ¹¹⁸ A. Bates, A. Daducci, and E. Caruyer (Proc Intl Soc Mag Reson Med, 2019).
- ¹¹⁹ Y.-Q. Song and L. Xiao, *NMR in Biomedicine* **n/a**, e4238 (2020).